JAIST Repository
https://dspace.jaist.ac.jp/

Title	Molecular dynamics simulation of polymer electrolyte membrane for understanding structure and proton conductivity at various hydration levels using neural network potential
Author(s)	Taborosi, Attila; Aoki, Kentaro; Zettsu, Nobuyuki; Koyama, Michihisa; Nagao, Yuki
Citation	Macromolecules, 58(7): 3720-3727
Issue Date	2025-03-26
Type	Journal Article
Text version	author
URL	https://hdl.handle.net/10119/20327
Rights	Attila Taborosi, Kentaro Aoki, Nobuyuki Zettsu, Michihisa Koyama, Yuki Nagao, Macromolecules 2025, 58, 7, 3720–3727. This document is the Accepted Manuscript version of a Published Work that appeared in final form in Macromolecules, copyright (c) American Chemical Society after peer review and technical editing by the publisher. To access the final edited and published work see https://doi.org/10.1021/acs.macromol.4c02607.
Description	

JAIST
JAPAN
ADVANCED INSTITUTE OF
SCIENCE AND TECHNOLOGY

Japan Advanced Institute of Science and Technology

Molecular dynamics simulation of polymer electrolyte membrane for understanding structure and proton conductivity at various hydration levels using neural network potential

Attila Taborosi[1], Kentaro Aoki[2], Nobuyuki Zettsu[3,4], Michihisa Koyama[1], Yuki Nagao[2*]*

[1] Research Initiative for Supra-Materials, Shinshu University, 4-17-1 Wakasato, Nagano 380-8553, Nagano, Japan

[2] School of Materials Science, Japan Advance Institute of Science and Technology, 1-1 Asahidai, Nomi 923-1292, Ishikawa, Japan

[3] Institute for Aqua-Regeneration, Shinshu University, 4-17-1 Wakasato, Nagano 380-8553, Nagano, Japan

[4] Department of Materials Chemistry, Faculty of Engineering, Shinshu University, 4-17-1 Wakasato, Nagano 380-8553, Japan

for Table of Contents use only

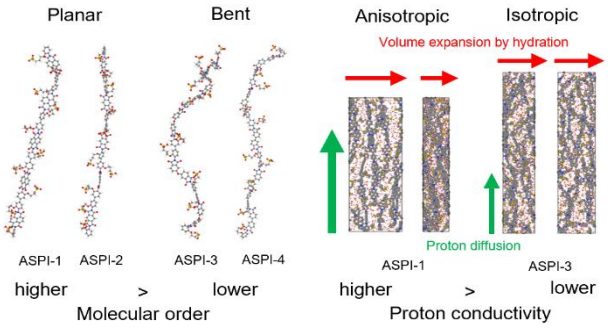

KEYWORDS polymer electrolyte, alkyl sulfonated polyimide, molecular dynamics, neural network potential, structural features, water uptake, proton conductivity

ABSTRACT Alkyl sulfonated polyimides (ASPIs), as alternative polymer electrolyte for fuel cells, are known to exhibit lyotropic liquid crystalline behavior upon water uptake, forming organized lamellar structures and achieving high proton conductivity. Previous experimental studies have shown that ASPIs with planar backbones exhibit enhanced proton conductivity (0.2 S/cm) compared to those with bent backbones (0.03 S/cm). To explain this difference at the atomistic level, molecular dynamics simulations were conducted using universal neural network potential. The appearance of monomer unit length in planar ASPIs, indicating higher molecular order, was found to correlate with higher proton conductivity compared to bent ASPIs. Despite the similar deprotonation and solvation of sulfonic acid groups in both planar and bent ASPIs, the proton conductivity was independent of these factors. Directional mean square displacement analysis provided further insights into the differences in the proton conductivity between planar and bent types.

1. Introduction

Perfluorinated sulfonic acids (PFSAs) such as Nafion, are popular polymer electrolytes for fuel cells with a hydrophobic backbone containing fluorine atoms and flexible side chains with ether and sulfonic acid groups (SO_3H).[1,2] Sulfonic acid groups are capable of binding water molecules through hydrogen bonds and through deprotonation of SO_3H groups, providing proton transport at high water content. However, PFSAs have limitations in high-temperature and low-humidity conditions, which have led to the development of alternative polymer electrolytes for fuel cells. Sulfonated polyimides (SPIs) have been studied as alternative electrolyte for fuel cells, because of their high chemical and thermal stability.[3–5] In previous experimental studies,[6–9] the thin film form of alkyl sulfonated polyimides (ASPIs) showed an anisotropic lyotropic lamellar structure, confirmed by humidity-controlled grazing incidence X-ray scattering (GI-XRS) measurements. This organized structure constructs long-range conduction paths[10], while the linear expansion of the lamellar structure and improved structural ordering was revealed from water uptake. This, resulted in high proton conduction up to 0.1 S/cm at 298 K and 95% relative humidity (RH) due to the smooth proton conduction along the polymer backbone. Furthermore, the degree of molecular order enhances the proton conductivity with increasing molecular weight.[8,11,12] Further study[7] was conducted to understand the effects of backbone modification for the design of ASPIs with enhanced proton conductivity.

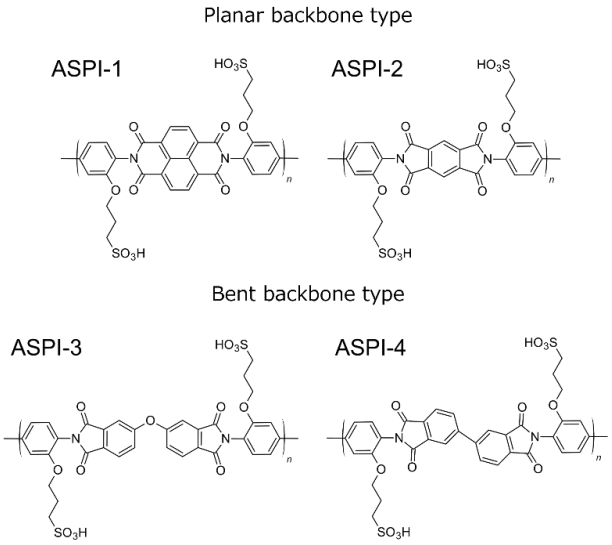

Figure 1. Chemical structures of planar (ASPI-1 and ASPI-2) and bent (ASPI-3 and ASPI-4) backbone ASPIs.

Thus, two types of backbones (Figure 1) were synthesized: planar (ASPI-1 and ASPI-2) and bent (ASPI-3 and ASPI-4) backbones. Both planar and bent exhibited a humidity induced lyotropic lamellar structure, and water uptake enhanced the molecular order via lamellar expansion. The backbone planarity affected the arrangement of interchain packing in the organized lamellar structure. ASPI forms a lyotropic lamellar phase in which the main chain and side chains are segregated. The arrangement of the main chain structure within the lamellar organization can be considered analogous to a thermotropic liquid crystal. This structure can be categorized into two types: one where the monomer units are aligned to form a hierarchical lamellar structure, resembling a main-chain smectic phase, and another where there is no distinct arrangement of the main chain, resembling a main-chain nematic phase. The planar ASPIs exhibited a smectic ordering and higher proton conductivity reaching 0.1 S/cm, while the bent ones showed a nematic ordering and lower proton conductivity (Table 1).

Table 1. Structural information[7] of planar (ASPI-1 and ASPI-2) and bent (ASPI-3 and ASPI-4) backbone ASPIs.

Entry	Type of backbone	Smectic /Nematic	Proton conductivity[1] [S/cm]	Lamellar distance[1] [Å]	Lamellar distance[2] [Å]
ASPI-1	Planar	Smectic	0.179	29	13
ASPI-2	Planar	Smectic	0.196	30	16
ASPI-3	Bent	Nematic	0.029	31	17
ASPI-4	Bent	Nematic	0.080	29	15

[1]at 298 K and 95% RH. [2]at 298 K and 5% RH.

Despite comprehensive experimental studies on the structure, water uptake, and proton conductivity of ASPIs, the lack of atomistic level understanding of these features and mechanisms prevents the rational and fast design of new types of ASPIs with enhanced proton conductivity. To fill this gap, we employed molecular dynamics (MD) simulations with universal neural network potential (UNNP) method to investigate and deepen our understanding on the structural, water uptake, and proton conductivity differences between planar and bent backbone ASPI types.

Several investigations have been conducted on the water uptake and proton transport mechanisms in PFSA and other electrolytes using various computational chemistry methods, including first-principles[13,14], semi-empirical[15], classical force-field[16], and coarse-grained[17] MD simulations. These studies provided valuable insights for simulating and analyzing water uptake and proton conductivity. However, considering both Grotthuss and vehicle mechanisms, the understanding of proton conductivity remains a complex and challenging task.

To elucidate the mechanism of proton conduction, Peterson *et al.*[18] utilized the empirical valence bond (EVB) approach to explore the Grotthuss mechanism in Nafion, uncovering a complex

interplay between vehicular and Grotthuss mechanisms that resulted in a relatively modest net proton diffusion rate. Luduena *et al.*[14] investigated the proton conduction in poly(vinyl phosphonic acid) using density functional theory (DFT) based MD simulations, highlighted the role of water molecules in facilitating local proton hopping (Grotthuss mechanism) and maintaining hydrogen-bonding networks. Zhang *et al.*[19], using reactive force field (ReaxFF) MD simulations to treat Grotthuss mechanism, focused on amine-based membranes and examined how different functional groups and polymer backbones influence the proton conductivity. Recent advances by Mabuchi *et al.*[20–22] using a modified EVB approach on PFSA have provided further insights into proton conductivity, considering both Grotthuss and vehicle mechanisms. Among the abovementioned methods, we decided to use UNNP method in this study, which offers a promising opportunity to simulate proton conductivity at a new level, enabling long-timescale simulations that incorporate both mechanisms.

Koyama *et al.*[13] conducted DFT calculations on CF_3SO_3H and CH_3SO_3H, highlighting the superior proton dissociation and hydration properties of hydrocarbon-based sulfonic acids under low humidity conditions. Pozuelo *et al.*[16] employed classical MD simulations to reveal the enhanced naked proton diffusion compared to hydrated protons in sulfonated poly(phenyl sulfone). Further classical MD simulations by Park *et al.*[23] compared PFSA and SPI, identified differences in water channel formation and phase separation that impact the proton transport. Furthermore, Ohkubo *et al.*[24] and Bahlakeh *et al.*[25] investigated the structural and transport properties of Nafion, sulfonated polyether sulfone, and sulfonated poly(ether ketone), to elucidate the effects of hydration and the degree of sulfonation on membrane performance. Hu *et al.*[17] used dissipative particle dynamics (DPD) on PFSA and SPI provided further insights into the mechanisms of water uptake. However,

to the best of authors' knowledge, no molecular level investigation has been performed on ASPIs to date.

2. Methodology

2.1 Computational

2.2.1 Simulation details

The simulations were performed using the UNNP called PreFerred Potential[26] (PFP) version 4.0, including dispersion correction D3[27], using the Atomic Simulation Environment [28] implemented in Matlantis[29] software package. The simulation results were visualized by Chemcraft[30] and Ovito[31] software. A systematic simulation process was carried out to prepare the equilibrated bulk phase for the four different ASPIs (Figure 1). We created a single polymer chain with five repeating units (n = 5) (Figure S1), and each initial simulation box was constructed using five single polymer chains, which were randomly placed along *a* and *b* axes and aligned in the direction of the *c* axis (Figure S2). Furthermore, the *c* axis of the simulation box was different from the *a* and *b* axes (60 Å), considering the length of the pentamer units for the initial simulation box. Therefore, the initial *c* axis was set to 80 Å for ASPI-1 and ASPI-2, while it was set to 100 Å for ASPI-3 and ASPI-4. Geometry optimization using the Fast Inertial Relaxation Engine (FIRE) algorithm was performed with f_{max} = 0.1 convergence threshold, followed by 50 ps NVE calculation to prepare the initial configuration for the equilibration process, inspired by a previously reported[32,33] 21-step equilibration process for polymers. Considering the size of the system (nearly 2000 atoms), the limitations of PFP, and the excessive calculation time, we performed only 6-step equilibration process (Table S1) with shorter simulation time for each ASPIs. Each 100 ps NVT calculation at 298 K was followed by a 100 ps NPT simulation at the

same temperature, initially applying 100 bar pressure only on the *a* and *b* axes, then decreasing it to 50 and 1 bar, applying pressure on all axes (Table S1, Eq. ver. 1). Furthermore, additional 6-step equilibration processes (Table S1, Eq. ver. 2 and Eq. ver. 3) with higher temperature (650 and 1000 K) and higher pressure (300 and 150 bar) were also performed, however without significant changes in the equilibration results (Figure S3 and S4). This procedure allowed for the formation of polymer into a lamellar structure. After the 6-step equilibration process, a 500 ps NVT production simulation was performed to determine the dry bulk phase. The last snapshot of the equilibrated bulk phase of ASPIs is shown in Figure S3.

The different hydration level simulations were carried out using the last snapshot of the 500 ps NVT production simulation of the bulk phase to gain insight into the volume expansion and proton conductivity upon water uptake derived from lyotropic liquid crystalline properties. These simulations were performed only ASPI-1 and ASPI-3 due to computational time constraints. First 100 water molecules were randomly placed into the system, achieving water uptake per sulfonic acid group of λ = 2 (100 H_2O/50 SO_3H). Geometry optimization of the entire system was then performed using the FIRE algorithm with f_{max} = 0.1 convergence threshold. The equilibration process was performed with a 50 ps NVT calculation at 298 K, followed by a 100 ps NPT simulation at 1 bar on the same temperature, while applying pressure on all axes of the simulation box, and a final 50 ps NVT simulation (Table S2, 3-step). Two additional equilibration processes were also performed, incorporating the 6-step equilibration process with room (Table S2, 6-step ver. 1) and higher temperature (Table S2, 6-step ver. 2) for λ = 2. However, the difference within the equilibration results is not significant to perform longer equilibration time (Table S3). Based on 3-step equilibration process , this was repeated for λ = 4, 6, 8, 10, and 12, always using the last

snapshot of the previous equilibration process. Furthermore, 2 ns NVT production calculations at 298 K were performed for λ = 2, 6, and 12 for discussing the proton conductivity.

2.2.2 Analysis of the simulation results

The pairwise (N–N, S–O, S–S, C–O, O–H) radial distribution functions (RDF) were analyzed to determine the structural features in the dry and humidified states. Eq. (1) was used to determine the probability distribution of B atoms at a distance *r* from an A atom:

$$g_{\mathrm{A-B}}(r) = \frac{n_{\mathrm{B}}}{4\pi r^2 dr} \Big/ \frac{N_{\mathrm{B}}}{V} \quad (1)$$

where n_{B} is the number of B atoms located at a distance *r* in a shell with thickness *dr* from atom A, N_{B} is the total number of B atoms, and *V* is the total volume of the system. Furthermore, the coordination number (n_{B}) between A and B atoms was determined using Eq. (2):

$$n_{\mathrm{B}} = 4\pi \frac{N_{\mathrm{B}}}{V} \int r^2 g_{\mathrm{A-B}}(r) dr \quad (2)$$

All the pairwise RDFs were determined by the Ovito software using the coordination analysis and element-wise RDF.

The interaction energy (ΔE_{int}) was estimated for each ten snapshots of the whole 500 ps NVT product simulation and averaged with Eq. (3)

$$\Delta E_{\mathrm{int}} = E_{\mathrm{bulk}} - (E_{\mathrm{A}} + E_{\mathrm{B}}) \quad (3)$$

where E_{bulk} refers to the energy of the entire bulk phase, E_{A} corresponds to the energy of one single polymer chain, and E_{B} is the energy of the remaining four single polymer chain (Figure S6). Additional quasi-harmonic analysis was performed to calculate the free energy (ΔG), which results

are reported in the supporting information. The degrees of deprotonation of SO_3H for each λ were determined by dividing the average number of SO_3^- by the total number of S in the system. The SO_3^- group was judged to be fully deprotonated when the O–H distance exceeded over 1.1 Å.

The diffusion coefficient and proton conductivity were estimated from the mean square displacement (MSD) of both the Grotthuss and vehicle mechanisms. Proton hopping between H_3O^+ and H_2O, as well as between SO_3H and H_2O, was considered for the Grotthuss (*G*) mechanism, thus the MSD of the hydrogen atoms of these groups was calculated. For the vehicle (*V*) mechanism, the oxygen atoms of H_3O^+ were considered by identifying those bonded to three nearby hydrogen atoms within a bond distance of 1.1 Å. Proton hopping events were excluded by updating the reference oxygen atom when a proton switch occurred, ensuring that only vehicle transport was tracked. Therefore, the MSD of the oxygen atoms in the H_3O^+ were calculated. The MSD curves were determined using Eq (4):

$$MSD_{\mathrm{G/V}} = \frac{1}{N}\sum_{j=1}^{N}\left[\left(r_j(t) - r_j(0)\right)^2\right] \quad (4)$$

where N is the total number of atoms (Grotthuss and vehicle), and $r_j(t)$ and $r_j(0)$ are the positions at time t and the beginning of the simulation, respectively. The diffusion coefficients (D) of Grotthuss and vehicle were evaluated from the MSD curves (Einstein relation) based on Eq (5):

$$D_{\mathrm{G/V}} = \frac{1}{6N}\lim_{t\to\infty}\sum_{j=1}^{N}\left[\left(r_j(t) - r_j(0)\right)^2\right] \quad (5)$$

The Grotthuss and vehicle proton conductivity (σ_G and σ_V) was determined based on the Nernst-Planck ionic transport formalism[16] from the individual diffusion coefficients according to Eq (6), while the final proton conductivity was the sum of the individual proton conductivity values:

$$\sigma = \sum \sigma_{G/V} = \frac{Nz^2e^2D_{G/V}}{VkT} \quad (6)$$

where N is the number of hydrogen or hydronium atoms (N_H or N_{H3O} in Table S3), z is the charge number, and e is the elementary charge. V is the total volume of the system, T is the absolute temperature, and k is the Boltzmann constant. Please refer to the supporting information for further details regarding the values of each λ = 2, 6, 12 systems (Table S3). Furthermore, two alternative approaches were also considered to determine the diffusion coefficient and proton conductivity, which is discussed in the supporting information.

2.2 Experimental

The densities of ASPI-1 and ASPI-2 were estimated by X-ray reflectometry (XRR) using PANalytical X'Pert Pro MPD diffractometer with Cu $K\alpha$ radiation source. Each ASPI was dissolved in a mixed solvent of deionized water: THF (1:1), and spin coating was performed using the Motofit program package[34] using the generic algorithm in the *IGOR Pro*[35] environment. The densities of ASPI-3 and ASPI-4 were calculated using a custom designed in situ QCM system. The QCM substrate was connected to an oscillation circuit and frequency counter (5313A, Agilent Technologies) and set in a custom-built humidity chamber equipped with a high-resolution RH sensor (THQ-100P-SW; Tamadevice Co., Ltd, Japan). The area of the thin film was, where the films were scratched in a 5 mm Φ using a cotton swab moistened with a water/THF mixed solution. The thickness of the films was measured by scanning the height profiles of the scratched films using Alpha-Step D-500 (KLA Tencor, USA). The weight m of the thin film was determined using the Sauerbrey's equation:

$$m = \frac{S\times\sqrt{\rho\mu}}{2\times F^2} \times (-\Delta F) \quad (6)$$

where S represents the electrode surface area, ρ and μ denote the quartz density and quartz shear modulus, F stands for the fundamental frequency of the QCM substrate, and ΔF represents the frequency difference before and after the fabrication of the ASPI thin film.

3. Results and discussion

3.1 Structural features of the bulk phase of ASPIs in under conditions

To validate the reliability of our computational models, we first compared the computed densities of the equilibrated forms of all ASPIs with the experimentally determined bulk densities. The computed density of the final equilibrated bulk showed similar values for all ASPIs, which were relatively high for ASPI-1 (1.34 g/cm^3) and ASPI-3 (1.30 g/cm^3) and low for ASPI-2 and ASPI-4 (1.28 g/cm^3) (Table 2, Figure S7). These values were slightly lower than the experimental results, where ASPI-1, 2, and 4 showed similar values (1.53-1.55 g/cm^3), while ASPI-3 was lower (1.47 g/cm^3). This nearly 0.2 g/cm^3 difference between the experimental and computational results was consistent with the results of a previous simulation study [36] on Nafion showing 0.2 g/cm^3 difference from the experimental values.

Table 2. Computational and experimental density results for the different ASPIs.

Entry	Computed Density [g/cm^3]	Experimental Density [g/cm^3]
ASPI-1	1.34	1.55±0.03
ASPI-2	1.28	1.53±0.04
ASPI-3	1.30	1.47±0.02
ASPI-4	1.28	1.54±0.02

The N–N RDF was used to characterize the structural features of both the single polymer chain and the bulk phase of ASPIs. The single polymer chain analysis revealed the key units of the

polymer chains based on the 1st, 2nd, and 3rd nearest neighbor distances between the backbone nitrogen atoms (Figure 2). Thus, we distinguished three main units with specific distances for each ASPI, namely the dianhydride, biphenyl, and monomer units. The N–N distance of the biphenyl units was 10 Å for all ASPIs, while the dianhydride and monomer unit distances varied depending on the ASPIs. ASPI-1 and ASPI-2 showed shorter distances for both the dianhydride and monomer units, while ASPI-3 and ASPI-4 showed longer distances (Figure 2).

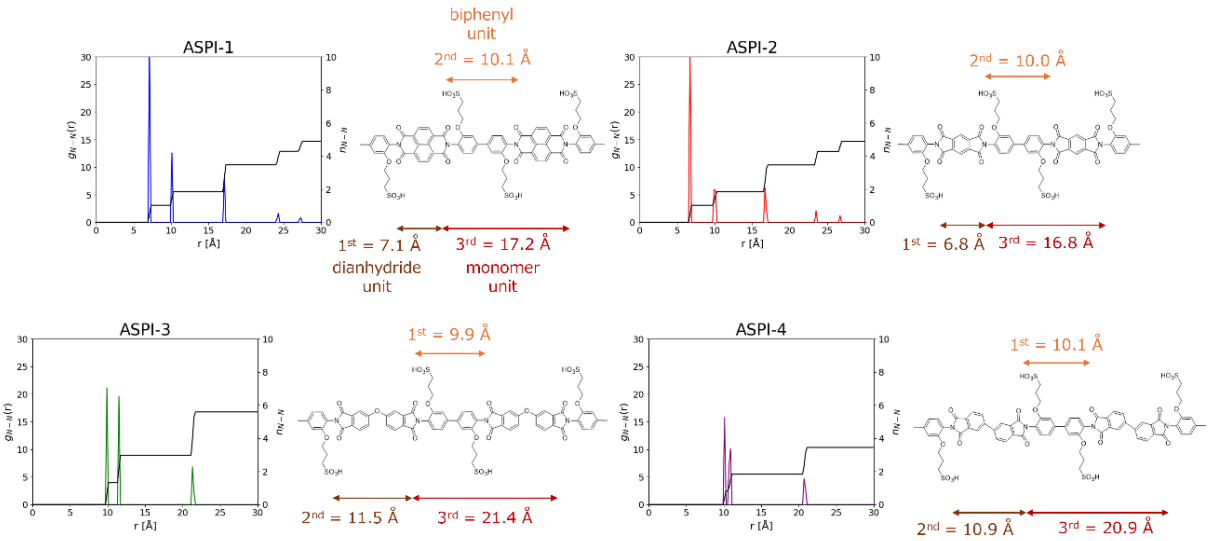

Figure 2. The N–N RDF for the single polymer chains (n = 5) of ASPIs to define the key units within the single polymer chain.

The single polymer chain structure analysis was utilized to distinguish the complex features of the bulk phase. The bulk phase N–N RDF showed similarities to the single polymer chain N–N RDF (Figure 3), allowing us to assign the three units of the single polymer chain. We confirmed the dianhydride unit of ASPI-1 and ASPI-2 at 7 Å, that of ASPI-3 and ASPI-4 at 11 Å and the biphenyl unit at 10 Å for all ASPIs. However, a key difference was found for the monomer unit: ASPI-1 and ASPI-2 showed $g_{N–N}$ peaks at 17 Å, while this peak was not observed for ASPI-3 and ASPI-4

at 21 Å (Figure 3). Our previous experimental results of GI-XRS[7] were similar to these observations, as the scattering peaks derived from monomer unit length were observed in planar backbones ASPIs (ASPI-1 and ASPI-2) at 16 Å along the polymer chain, while the scattering peak was absent in bent ones (ASPI-3 and ASPI-4). The former ASPIs can be attributed to the smectic ordering, while the latter ones are to the nematic ordering, respectively. Therefore, our calculation results successfully reproduced the smectic/nematic ordering of the planar (ASPI-1 and ASPI-2) and bent (ASPI-3 and ASPI-4).

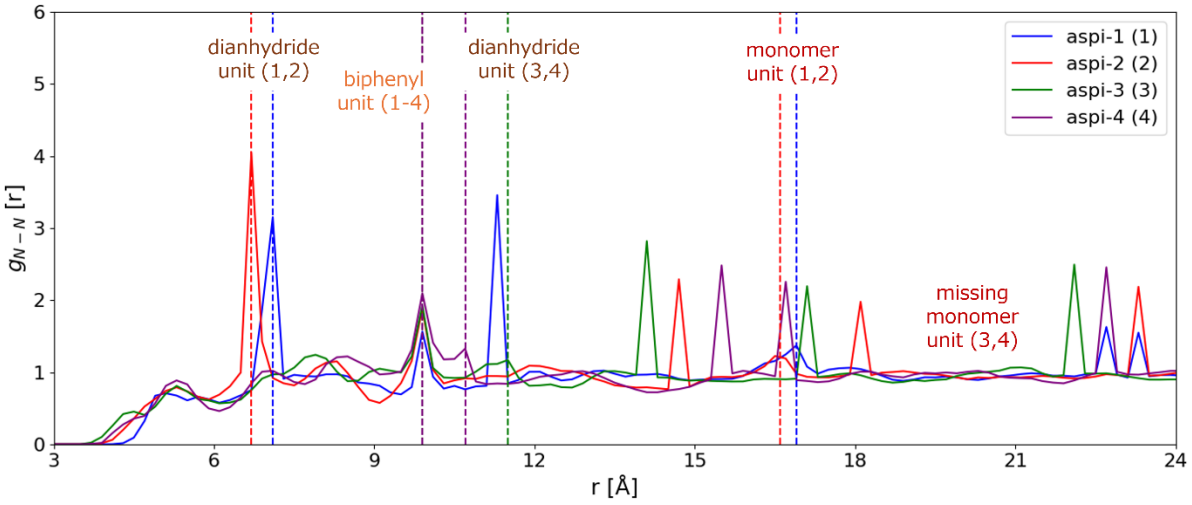

Figure 3. The N-N RDF for the bulk phase of ASPIs, where the dashed lines indicate the single polymer chain units (dianhydride, biphenyl, and monomer). The additional peaks are artifacts arising from the boundaries of the simulation box.

Besides the single polymer unit g_{N-N} peaks, we observed additional peaks with significant probability intensities at 10-24 Å range. These peaks are artifacts arising from the boundaries of the simulation box. Based on the GI-XRS results, ASPI-1 showed a shorter lamellar distance (13 Å), while ASPI-2, 3, and 4 showed longer distances (16 Å) under dry conditions. To gain insights into the shorter lamellar distance in ASPI-1, we calculated the interaction energies between

individual polymer chains in the bulk phase. The interaction energy can be used to quantify the different noncovalent interactions (H-bond, π–π, CH–π etc.) between polymer chains. ASPI-1 showed stronger interaction energy, while ASPI-2, -3, and -4 showed weaker interaction energies (Figure S8). This could be one of the explanations for the difference in the lamellar distances, as the stronger noncovalent interactions between the polymer chains could shorten the lamellar distance in ASPI-1.

3.2 The effect of hydration level on the structural features

The densities of ASPI-1 and -3 showed a decreasing trend upon increasing hydration level (Figure S9) as in previous computational studies.[19,36,37] Understanding how the hydration level affects the structural features of ASPIs is crucial for optimizing the proton conductivity. The N–N distances of the dianhydride, biphenyl, and monomer units of the single polymer chain were not affected by the water content (λ) regardless of the ASPIs (Figure S10).

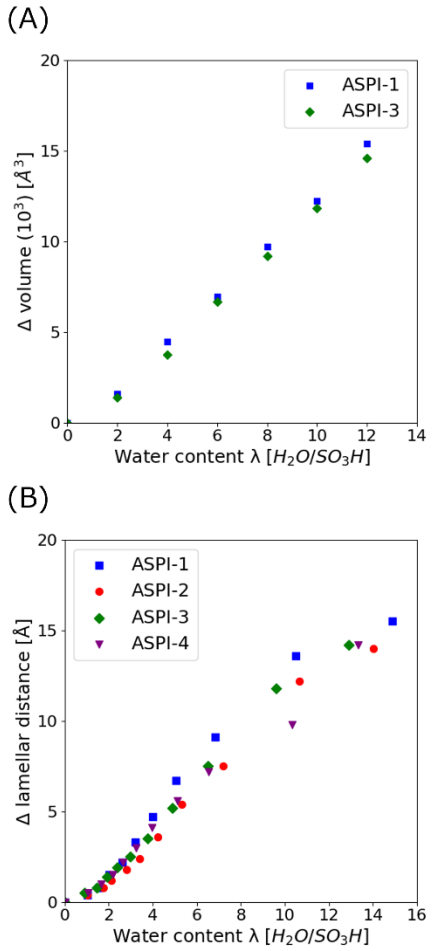

Figure 4. Change of the volume and lamellar distance in function of hydration level (λ) from computational simulations (A) and experimental investigations[7] (B).

The expansion of the lattice parameters and cell volume of the bulk phases of ASPI-1 and -3 are shown in Figure 4A and S11. The volume expansion of each hydration level was similar between ASPI-1 and ASPI-3 and showing similar linear increasement trends as the experimental lamellar distance upon water uptake (Figure 4B). ASPI-1 and -3 showed different tendencies in expansion, thus *a* and *b* axes expanded simultaneously in ASPI-3, while *b* axis expanded preferentially compared with *a* axis in ASPI-1. This can be explained by the previously discussed interaction energy, as the stronger noncovalent interactions in ASPI-1 prevent the water diffusion between

polymer chains, thus causing pronounced expansion in one direction. The expansion of the *c* axis was not significant compared to the *a* and *b* axes, and no differences were found between the two ASPIs in this regard.

Furthermore, the S–S and S–O RDF analyses provided information regarding changes in the sulfonic acid group upon water uptake. The S–S RDF was investigated to gain insights into the hydration of SO_3H (Figure S12). The splitting of the $g_{S–S}$ peak was observed at 5 Å for both ASPI-1 and -3 by hydration, implying the solvation of sulfonic acid, as the distance increased between the two sulfur atoms of SO_3H upon interaction with water. The S–O RDF showed that the first $g_{S–O}$ double peak changed into a single peak for both ASPI-1 and -3 (Figure S13), indicating the deprotonation of SO_3H during solvation. The S–O distances in SO_3H in the presence of a proton can be divided into two short (S=O, 1.50 Å) and one long (S–OH, 1.55 Å) distances, which upon deprotonation change into three similar distances (1.50 Å). The second coordination environment of S···O is the interaction between SO_3H and backbone C=O or another SO_3H at dehydrated state. After hydration, the SO_3^- group interacts only with the coordinated water, and the S···O distance increases from 3.5 to 3.8 Å. Furthermore, the water uptake also affected the deprotonation of sulfonic acid, with almost 90% of the SO_3^- form being achieved, reaching saturation at $\lambda > 8$ (Figure S14). The C–O RDF (Figure S15), O–H RDF (Figure S16), and O–O RDF (Figure S17) analyses provided further information regarding the structural changes, which is discussed in the supporting information. Overall, no differences, except for the dimensional expansion were observed between ASPI-1 and -3 regarding the solvation of the sulfonic acid group. This suggests that the experimental differences in proton conductivity are not related to the deprotonation mechanism or solvation of the sulfonic acid groups.

3.3 Diffusion coefficient and proton conductivity

To assess the impact of water uptake on proton transport, the diffusion coefficient (D) was determined separately for the Grotthuss (D_G) and vehicle mechanisms (D_V) in function of water uptake in the planar and bent ASPIs (Figure 5A, see also Figure S21A). The D_G and D_V values were derived from the regime of MSD (Grotthuss and vehicle) curves between 0.5 and 1.8 ns (Figure S18). The MSD of the Grotthuss mechanism was higher than that of the vehicle mechanism. Therefore, the determined D values diverged between the two mechanisms, regardless of the ASPI type, which is in good agreement with the previous Nafion experimental[38] and computational[18,21] findings. Furthermore, differences were found in the MSD (Grotthuss and vehicle) and determined D values of ASPI-1 and -3. At low water contents (λ = 2), the D values were similar (0.34 x 10^{-6} cm^2/sec), while at high water contents (λ = 12), the D values were almost double for ASPI-1 (0.97 x 10^{-6} cm^2/sec) compared to ASPI-3 (0.56 x 10^{-6} cm^2/sec) (Figure 5A).

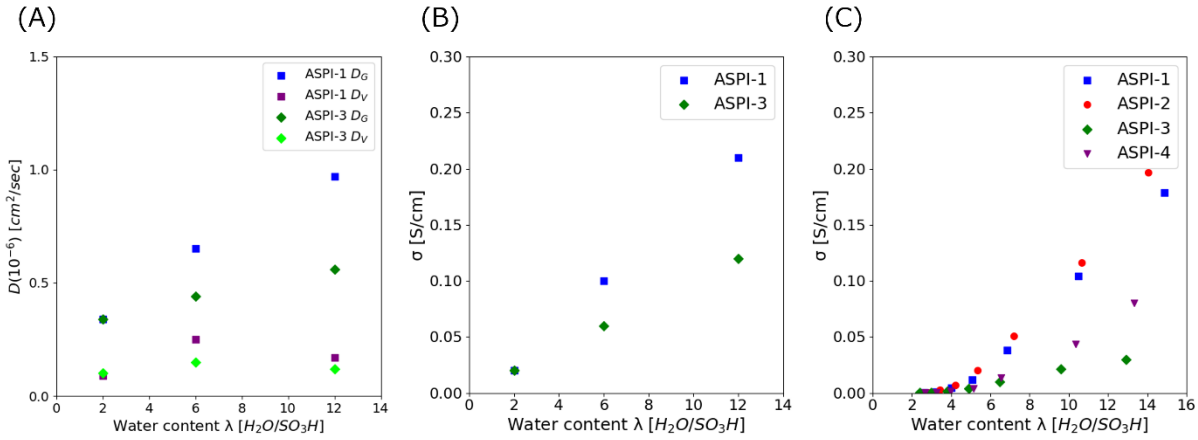

Figure 5. The diffusion coefficient (D) and proton conductivity (σ) in the function of water uptake (λ) for ASPI-1 and -3 from computational simulations (A, B) and experimental investigations[7] (C).

The proton conductivity (σ) was calculated based on Eq. (5) from D_G and D_V (Figure 5B, see also Figure S21B). We observed an increase in the proton conductivity as a function of the water uptake, consistent with our previous experimental results[7] (Figure 5C, see also Figure S21C). Furthermore, the proton conductivity of ASPI-1 was higher than that of ASPI-3 upon increasing water content, confirming our experimental observations. Upon λ = 12 the ASPI-1 and -3- showed 0.21 and 0.12 S/cm, respectively (Figure 5B). Although higher than the experimental values of ASPI-1 (0.18 S/cm) and -3 (0.03 S/cm), a similar trend was observed. The experimental difference in the proton conductivity between ASPI-1 and -3 was sixfold at high water contents, whereas the computational difference was only twofold. The discrepancies between the experimental and computational results could be due to the limitations in modelling (such as the length and number of polymer chains in the simulation box), the short time scale (2 ns NVT) of the MD simulation, which is unable to catch the long-time diffusion or to overcome the caging effects of proton, atom selection method for Grotthuss and vehicle mechanisms, or the use of Eq. (5) to determine the proton conductivity. The directional (*a*, *b*, *c* axes) MSD analysis at λ = 12 further revealed differences between ASPI-1 and -3 (Figure S19). Thus, the diffusion of H and O atoms of ASPI-1 was higher along the *c* axis (along the polymer chain) than along the *a* or *b* axis, whereas this distinction was not observed for ASPI-3. Therefore, the planar backbone structure of ASPI-1, which showed consistent monomer unit lengths in both experimental and computational results, promoted diffusion along the polymer chain direction, unlike ASPI-3 with its bent backbone structure.

4. Conclusion

In this study, we performed MD simulations using the UNNP method to understand the structural, water uptake, and proton conductivity differences between ASPIs with planar and bent backbone. The appearance of monomer units, indicating high molecular order, in planar ASPIs (ASPI-1 and

ASPI-2) suggest a better proton conductivity compared to bent ones (ASPI-3 and ASPI-4). Furthermore, the computational findings of these structural differences between the ASPIs were in good agreement with previous experimental results.[7] Water uptake simulations suggest that the difference in proton conductivity between planar (ASPI-1) and bent (ASPI-3) ASPIs is not related to the deprotonation or solvation of the sulfonic acid group. However, the directional MSD analysis revealed that H and O atoms diffusion was greater along the polymer chain in planar than bent, explaining the difference in proton conductivity, which is related to the higher molecular order of planar types. Finally, the use of the UNNP method revealed that the Grotthuss mechanism became dominant over the vehicle mechanism at high water contents regardless of ASPIs. These results provide valuable guidance for the design of ASPI materials with improved proton conductivity.

ASSOCIATED CONTENT

Supporting Information

Details about molecular dynamics simulation steps, parameters to determine the proton conductivity, snapshot of initial and equilibrated bulk phase of ASPIs, determination of interaction energy and free energy, average interaction energies for ASPIs, density change during equilibration and water uptake, element pairwise RDF, the expansion of volume during water uptake, formation of SO_3^- during water uptake, alternative approaches to determine diffusion coefficient and proton conductivity, MSD and directional MSD of H and O atoms, snapshots of different hydration levels of ASPIs

AUTHOR INFORMATION

Corresponding Author

*E-mail: taborosi_attila@shinshu-u.ac.jp (A.T.), ynagao@jaist.ac.jp (Y. N.)

Author Contributions

The manuscript was written through contributions of all authors. All authors have given approval to the final version of the manuscript.

ORCID

Attila Taborosi: 0000-0003-3339-6745

Kentaro Aoki: 0000-0003-4148-6070

Nobuyuki Zettsu: 0000-0003-2838-3165

Michihisa Koyama: 0000-0003-4347-9923

Yuki Nagao: 0000-0003-1249-440X

Notes

The authors declare no competing financial interest.

ACKNOWLEDGMENT

This work was supported by JST CREST (Grant No. JPMJCR21B3), Japan.

ABBREVATIONS

PFSA, Perfluorinated sulfonic acid; SPI, Sulfonated polyimide; GI-XRS, grazing incidence X-ray scattering; RH, relative humidity; ASPI, alkyl sulfonated polyimide; MD, molecular dynamics; UNNP, universal neural network potential; EVB, empirical valence bond; DFT, density functional theory; DPD, dissipative particle dynamics; FIRE, fast inertial relaxation engine; XRR, X-ray reflectometry

REFERENCES

(1) Mauritz, K. A.; Moore, R. B. State of Understanding of Nafion. *Chem. Rev.* **2004**, *104*(10), 4535–4585. DOI: 10.1021/cr0207123.

(2) Kusoglu, A.; Weber, A. Z. New Insights into Perfluorinated Sulfonic-Acid Ionomers. *Chem. Rev.* **2017**, *117*(3), 987–1104. DOI: 10.1021/acs.chemrev.6b00159.

(3) Vallejo, E.; Pourcelly, G.; Gavach, C.; Mercier, R.; Pineri, M. Sulfonated Polyimides as Proton Conductor Exchange Membranes. Physicochemical Properties and Separation H^+/M^{Z+} by Electrodialysis Comparison with a Persuorosulfonic Membrane. *J. Membr. Sci.* **1999**, 160(1), 127-137, DOI: 10.1016/S0376-7388(99)00070-8

(4) Fang, J.; Guo, X.; Harada, S.; Watari, T.; Tanaka, K.; Kita, H.; Okamoto, K. Novel Sulfonated Polyimides as Polyelectrolytes for Fuel Cell Application. 1. Synthesis, Proton Conductivity, and Water Stability of Polyimides from 4,4'-Diaminodiphenyl Ether-2,2′-Disulfonic Acid. *Macromolecules* **2002**, *35*(24), 9022–9028. DOI: 10.1021/ma020005b.

(5) Miyatake, K.; Asano, N.; Watanabe, M. Synthesis and Properties of Novel Sulfonated Polyimides Containing 1,5-Naphthylene Moieties. *J. Polym. Sci. A Polym. Chem.* **2003**, *41*(24), 3901–3907. DOI: 10.1002/pola.10988.

(6) Krishnan, K.; Iwatsuki, H.; Hara, M.; Nagano, S.; Nagao, Y. Proton Conductivity Enhancement in Oriented, Sulfonated Polyimide Thin Films. *J. Mater. Chem. A.* **2014**, *2*(19), 6895–6903. DOI: 10.1039/C4TA00579A.

(7) Ono, Y.; Goto, R.; Hara, M.; Nagano, S.; Abe, T.; Nagao, Y. High Proton Conduction of Organized Sulfonated Polyimide Thin Films with Planar and Bent Backbones. *Macromolecules*. **2018**, *51*(9), 3351–3359. DOI: 10.1021/acs.macromol.8b00301.

(8) Yao, Y.; Watanabe, H.; Hara, M.; Nagano, S.; Nagao, Y. Lyotropic Liquid Crystalline Property and Organized Structure in High Proton-Conductive Sulfonated Semialicyclic Oligoimide Thin Films. *ACS Omega*. **2023**, *8*(8), 7470–7478. DOI: 10.1021/acsomega.2c06398.

(9) Nagao, Y. Progress on Highly Proton-Conductive Polymer Thin Films with Organized Structure and Molecularly Oriented Structure. Taylor and Francis Ltd. *Sci. Technol. Adv. Mater.* **January 1, 2020**, 21(1), 79–91. DOI: 10.1080/14686996.2020.1722740.

(10) Nagao, Y. Advancing Sustainable Energy: Structurally Organized Proton and Hydroxide Ion-Conductive Polymers. Elsevier B.V. *Current Opinion in Electrochemistry*. **April 1, 2024**, 44. DOI: 10.1016/j.coelec.2024.101464.

(11) Krishnan, K.; Iwatsuki, H.; Hara, M.; Nagano, S.; Nagao, Y. Influence of Molecular Weight on Molecular Ordering and Proton Transport in Organized Sulfonated Polyimide Thin Films. *J. Phys. Chem. C*. **2015**, *119*(38), 21767–21774. DOI: 10.1021/acs.jpcc.5b03292.

(12) Takakura, K.; Ono, Y.; Suetsugu, K.; Hara, M.; Nagano, S.; Abe, T.; Nagao, Y. Lyotropic Ordering for High Proton Conductivity in Sulfonated Semialiphatic Polyimide Thin Films. *Polym. J.* **2019**, *51*(1), 31–39. DOI: 10.1038/s41428-018-0111-1.

(13) Koyama, M.; Bada, K.; Sasaki, K.; Tsuboi, H.; Endou, A.; Kubo, M.; Del Carpio, C. A.; Broclawik, E.; Miyamoto, A. First-Principles Study on Proton Dissociation Properties of Fluorocarbon- And Hydrocarbon-Based Membranes in Low Humidity Conditions. *J. Phys. Chem. B*. **2006**, *110*(36), 17872–17877. DOI: 10.1021/jp060281i.

(14) Ludueña, G. A.; Kühne, T. D.; Sebastiani, D. Mixed Grotthuss and Vehicle Transport Mechanism in Proton Conducting Polymers from Ab Initio Molecular Dynamics Simulations. *Chem. Mater.* **2011**, *23*(6), 1424–1429. DOI: 10.1021/cm102674u.

(15) Knaup, J. M.; Tölle, P.; Köhler, C.; Frauenheim, T. Quantum Mechanical and Molecular Mechanical Simulation Approaches Bridging Length and Time Scales for Simulation of Interface Reactions in Realistic Environments. *Eur. Phys. J. Spec. Top.* **2009**, *177*(1), 59–81. DOI: 10.1140/epjst/e2009-01168-5.

(16) Pozuelo, J.; Riande, E.; Saiz, E.; Compañ, V. Molecular Dynamics Simulations of Proton Conduction in Sulfonated Poly(Phenyl Sulfone)s. *Macromolecules*. **2006**, *39*(25), 8862–8866. DOI: 10.1021/ma062070h.

(17) Hu, C.; Lu, T.; Guo, H. Mesoscale Modeling of Sulfonated Polyimides Copolymer Membranes: Effect of Sequence Distributions. *J. Membr. Sci.* **2018**, *564*, 146–158. DOI: 10.1016/j.memsci.2018.07.008.

(18) Petersen, M. K.; Voth, G. A. Characterization of the Solvation and Transport of the Hydrated Proton in the Perfluorosulfonic Acid Membrane Nafion. *J. Phys. Chem. B*. **2006**, *110*(37), 18594–18600. DOI: 10.1021/jp062719k.

(19) Zhang, W.; Van Duin, A. C. T.; ReaxFF Reactive Molecular Dynamics Simulation of Functionalized Poly(Phenylene Oxide) Anion Exchange Membrane. *J. Phys. Chem. C*. **2015**, *119*(49), 27727–27736. DOI: 10.1021/acs.jpcc.5b07271.

(20) Mabuchi, T.; Tokumasu, T. Molecular Dynamics Simulation of Proton Transport in Polymer Electrolyte Membrane. *J. Nanosci. Nanotechnol.* **2015**, *15*(4), 2958–2963. DOI: 10.1166/jnn.2015.9647.

(21) Mabuchi, T.; Tokumasu, T. Relationship between Proton Transport and Morphology of Perfluorosulfonic Acid Membranes: A Reactive Molecular Dynamics Approach. *J. Phys. Chem. B*. **2018**, *122*(22), 5922–5932. DOI: 10.1021/acs.jpcb.8b02318.

(22) Mabuchi, T. Revealing the Anticorrelation Behavior Mechanism between the Grotthuss and Vehicular Diffusions for Proton Transport in Concentrated Acid Solutions. *J. Phys. Chem. B*. **2022**, *126*(17), 3319–3326. DOI: 10.1021/acs.jpcb.1c09742.

(23) Park, C. H.; Lee, C. H.; Sohn, J. Y.; Park, H. B.; Guiver, M. D.; Lee, Y. M. Phase Separation and Water Channel Formation in Sulfonated Block Copolyimide. *J. Phys. Chem. B*. **2010**, *114*(37), 12036–12045. DOI: 10.1021/jp105708m.

(24) Ohkubo, T.; Kidena, K.; Takimoto, N.; Ohira, A. Molecular Dynamics Simulations of Nafion and Sulfonated Polyether Sulfone Membranes. I. Effect of Hydration on Aqueous Phase Structure. *J. Mol. Model.* **2011**, *17*(4), 739–755. DOI: 10.1007/s00894-010-0767-8.

(25) Bahlakeh, G.; Nikazar, M.; Hafezi, M. J.; Dashtimoghadam, E.; Hasani-Sadrabadi, M. M. Molecular Dynamics Simulation Study of Proton Diffusion in Polymer Electrolyte Membranes Based on Sulfonated Poly (Ether Sadr Abadi Ketone). *Int. J. Hydrog. Energy*. **2012**, *37*(13), 10256–10264. DOI: 10.1016/j.ijhydene.2012.03.004.

(26) Takamoto, S.; Shinagawa, C.; Motoki, D.; Nakago, K.; Li, W.; Kurata, I.; Watanabe, T.; Yayama, Y.; Iriguchi, H.; Asano, Y.; Onodera, T.; Ishii, T.; Kudo, T.; Ono, H.; Sawada, R.; Ishitani, R.; Ong, M.; Yamaguchi, T.; Kataoka, T.; Hayashi, A.; Charoenphakdee, N.; Ibuka, T. Towards Universal Neural Network Potential for Material Discovery Applicable to Arbitrary Combination of 45 Elements. *Nat. Commun.* **2022**, *13*(1), 2991. DOI: 10.1038/s41467-022-30687-9.

(27) Grimme, S.; Antony, J.; Ehrlich, S.; Krieg, H. A Consistent and Accurate Ab Initio Parametrization of Density Functional Dispersion Correction (DFT-D) for the 94 Elements H-Pu. *J. Chem. Phys.* **2010**, *132*(15), 154104. DOI: 10.1063/1.3382344.

(28) Apelgren, P.; Amoroso, M.; Säljö, K.; Montelius, M.; Lindahl, A.; Stridh Orrhult, L.; Gatenholm, P.; Kölby, L.; Arulkumar, S.; Parthiban, S.; Goswami, A.; Varma, R. S.; Naushad, M.; Gawande, M. B.; Lipskas, J.; Deep, K.; Yao, W.; Grogan, S. P.; Dorthé, E. W.; Glembotski, N. E.; Gaul, F.; D'Lima, D. D.; Beketov, E. E.; Isaeva, E. V.; Yakovleva, N. D.; Demyashkin, G. A.; Arguchinskaya, N. V.; Kisel, A. A.; Lagoda, T. S.; Malakhov, E. P.; Kharlov, V. I.; Osidak, E. O.; Domogatsky, S. P.; Ivanov, S. A.; Shegay, P. V.; Kaprin, A. D.; Sun, Y.; Wu, Q.; Zhang, Y.; Dai, K.; Wei, Y.; Dhawan, A.; Kennedy, P. M.; Rizk, E. B.; Ozbolat, I. T.; Ma, K.; Zhao, T.; Yang, L.; Wang, P.; Jin, J.; Teng, H.; Xia, D.; Zhu, L.; Li, L.; Jiang, Q.; Wang, X.; Fiscale, C.; In, R. E-Mail, I; Personal, S; Credit, S.; Trattamento. *T D*. E. L.; Tel, T.; Della, R.; Dei, P.; Adempiere, D. I.; Un, A. D.; Di, O.; Salvatore, D. A. The Atomic Simulation Environment—a Python Library for Working with Atoms. *Journal of Physics: Condensed Matter* 2017, *27*, 273002.

(29) Matlantis. https://Matlantis.Com/. *Software as a Service Style Material Discovery Tool*.

(30) Chemcraft. https://www.chemcraftprog.com. *Graphical Software for Visualization of Quantum Chemistry Computations*.

(31) Stukowski, A. Visualization and Analysis of Atomistic Simulation Data with OVITO-The Open Visualization Tool. *Modelling Simul. Mater. Sci. Eng.* **2010**, *18*(1). DOI: 10.1088/0965-0393/18/1/015012.

(32) Abbott, L. J.; Hart, K. E.; Colina, C. M. Polymatic: A Generalized Simulated Polymerization Algorithm for Amorphous Polymers. *Theor. Chem. Acc.* **2013**, *132*(3), 1–19. DOI: 10.1007/s00214-013-1334-z.

(33) Chakraborty, S.; Lim, F. C. H.; Ye, J. Achieving an Optimal T_g Change by Elucidating the Polymer-Nanoparticle Interface: A Molecular Dynamics Simulation Study of the

Poly(Vinyl Alcohol)-Silica Nanocomposite System. *J. Phys. Chem. C*. **2019**, *123*(39), 23995–24006. DOI: 10.1021/acs.jpcc.9b05545.

(34) Nelson, A. Co-refinement of Multiple-Contrast Neutron/X-ray Reflectivity Data Using MOTOFIT. *J. Appl. Crystallogr.* **2006**, *39*(2), 273–276. DOI: 10.1107/S0021889806005073.

(35) Igor Pro. https://www.wavemetrics.com (accessed 2024-09-19).

(36) Rohilla, T.; Husain, A.; Singh, N.; Mahajan, D. K. Atomistic Simulation and Synthesis of Novel Sulfonated Polyimide Polymer Electrolyte Membranes with Facile Proton Transport. *Chem. Eng. J.* **2023**, *474*. DOI: 10.1016/j.cej.2023.145727.

(37) Li, X.; Zhao, Y.; Wang, S.; Xie, X. Molecular Dynamics Simulation Study of a Polynorbornene-Based Polymer: A Prediction of Proton Exchange Membrane Design and Performance. *Int. J. Hydrog. Energy*. **2016**, *41*(36), 16254–16263. DOI: 10.1016/j.ijhydene.2016.05.254.

(38) Choi, P.; Jalani, N. H.; Datta, R. Thermodynamics and Proton Transport in Nafion. *J. Electrochem. Soc.* **2005**, *152*(3), E123. DOI: 10.1149/1.1859814.